Aalborg Universitet

AALBORG UNIVERSITY

Main Issues in the Synthesis and Testing of Thermocatalytic Ce-Doped SrFeO3 Perovskites for Wastewater Pollutant Removal

Palma , Davide; Deganello, Francesca ; Liotta, Leonarda Francesca; La Parola, Valeria; Bianco Prevot, Alessandra; Malandrino, Mery; Laurenti, Enzo; Boffa, Vittorio; Magnacca, Giuliana

Link to publication from Aalborg University

Article

Main Issues in the Synthesis and Testing of Thermocatalytic Ce-Doped SrFeO₃ Perovskites for Wastewater Pollutant Removal

Davide Palma [1], Francesca Deganello [2], Leonarda Francesca Liotta [2], Valeria La Parola [2], Alessandra Bianco Prevot [1,*], Mery Malandrino [1], Enzo Laurenti [1], Vittorio Boffa [3] and Giuliana Magnacca [1,4]

1   Dipartimento di Chimica, Università di Torino, Via P. Giuria 7, 10125 Torino, Italy
2   Istituto per lo Studio dei Materiali Nanostrutturati (ISMN)—Consiglio Nazionale delle Ricerche, 90146 Palermo, Italy
3   Department of Chemistry and Biochemistry, Aalborgh University, 9220 Aalborg, Denmark
4   NIS and INSTM Reference Centre, Via P. Giuria 7, 10125 Torino, Italy
*   Correspondence: alessandra.biancoprevot@unito.it

Abstract: The effect of the synthesis and processing parameters on the thermocatalytic performance of Ce-doped SrFeO₃ inorganic perovskites was investigated to improve the reproducibility and reliability of the synthetic methodology and of the testing procedure. A structural, surface and redox characterization was performed to check the extent of variability in the chemical–physical properties of the prepared materials, revealing that a strict control of the synthesis parameters is indeed crucial to optimize the thermocatalytic properties of Ce-doped SrFeO₃ inorganic perovskites. The thermocatalytic tests, aimed to degrade organic pollutants in water, were performed using Orange II and Bisphenol A as target compounds, in view of a later technological application. The main issues in the synthesis and testing of Ce-doped SrFeO₃ perovskite thermocatalysts are highlighted and described, giving specific instructions for the resolution of each of them. A limited number of prepared materials showed an efficient thermocatalytic effect, indicating that a full gelification of the sol, an overstoichiometric reducer-to-oxidizer ratio, a nominal cerium content of 15 mol%, slightly higher than its solubility limit (i.e., 14 mol%), a pH of 6 and a thermal treatment at 800 °C/2 h are the best synthesis conditions to obtain an effective Ce-doped SrFeO₃ perovskite. Regarding the testing conditions, the best procedure is to follow the degradation reaction without any preconditioning with the pollutant at room temperature. The severe leaching of the active perovskite phase during tests conducted at acidic pH is discussed. Briefly, we suggest confining the application of these materials to a limited pH range. Variability between thermocatalysts prepared in two different laboratories was also checked. The issues discussed and the proposed solutions overcome some of the obstacles to achieving a successful scale up of the synthesis process. Our results were favorable in comparison to those in the literature, and our approach can be successfully extended to other perovskite catalysts.

Keywords: advanced oxidation processes; experimental protocols; heterogeneous catalysis; inorganic thermal activation; organic pollutants; perovskites; physico-chemical characterization; solution combustion synthesis; strontium ferrates; water treatment

1. Introduction

The global increase in the use of freshwater, resulting from population growth, economic development, and changes in consumption patterns, combined with the increasingly evident effects of climate change, has led to increased incidence of water stress and to situations of scarce water resources, even in non-intrinsically arid areas. The problem is not only quantitative but also qualitative, because in many areas of the planet, water use is not followed by a treatment that restores its initial quality, and even where treatments are applied, they are not always completely effective [1]. This has led to a progressive deterioration of water resources with heavy repercussions on the sustainability of our society. It is

therefore necessary to rethink water resource management, i.e., to make urban wastewater and industrial wastewater treatment more efficient and extend them worldwide, aiming for a transition from a linear model (capture, use, discharge) to a circular model that facilitates the "regeneration" and reuse of water, minimizing withdrawal from primary sources.

In this context, a crucial aspect is represented by the removal of anthropogenic contaminants of emerging concern (CECs) which are resistant to biological wastewater treatment and are detected at very low concentrations in surface water bodies (and in some cases, in groundwater) [2,3]. Despite the negative impact of these substances on ecosystems and human health, there is still no comprehensive European regulation; nonetheless, there is an increasing focus on their monitoring in anticipation of regulatory compliance. The effective and sustainable removal of CECs will contribute to the "circular" management of water, reducing the impact of climate change on water availability.

Among the possible approaches for CECs removal, the application of Advanced Oxidation Processes (AOPs) has gained interest among researchers [4,5]. AOPs rely on the generation of highly reactive species (above all $HO^{\bullet}$ radicals) which are able to initiate the degradation of pollutants, in many cases degrading through complete oxidation to CO_2, H_2O and inorganic ions [6,7]. Over the years, great attention has been devoted to the application of photocatalysis for CEC degradation, and a variety of novel materials have been prepared and tested [8]. The spectrum of photocatalysts is indeed wide, spanning from semiconductor oxides to composite materials, often aiming to optimize light harvesting [9–11]. One of the main drawbacks of AOPs, and this is especially true for photocatalysis, is that the generation of reactive species is mostly light assisted, thus introducing additional energy costs when artificial light is employed or infrastructural aspects in case of harvesting solar light. Other AOPs operating in dark conditions, on the other hand, typically require the addition of reagents (e.g., ozonation, Fenton process, peroxone).

Recently, the capability has been shown of perovskite-type mixed oxides to be thermally activated and to promote the degradation of organic compounds [12,13], as well as their capability of activating peroxymonosulfate (PMS) in AOPs, where both free and non-free radical pathways may occur [14]. Inorganic perovskite-type materials are a versatile and multifunctional class of mixed oxides with the general formula ABO_3, where A sites are occupied by larger cations, B sites are occupied by smaller cations, and O sites can be occupied by oxygen or by other anions [15]. Several papers rely on the use of $Sr_{0.85}Ce_{0.15}FeO_{3-\delta}$ perovskite, which has been successfully tested (i) for the degradation of model organic pollutants such as azo-dye Orange II [16], acid orange 8 (AO8) [17], Bisphenol A [18], and acetamiprid (AAP), (ii) for the abatement of oil residues in water [19], (iii) in combination with graphene oxide as the active layer deposited over commercial flat-sheet polyethersulfone nanofiltration membranes, yielding an improved catalytic activity for the abatement of bisphenol A [20], (iv) in a novel strategy for water purification that involves the integration of membrane filtration and thermocatalytic pollutants degradation, using an alumina tubular support coated with an Al_2O_3-doped NF silica layer for the filtration step, aiming to simultaneous degrade micropollutants and mitigate fouling [21], and (v) in an integrated process based on membrane distillation and thermocatalytic oxidation, simultaneously using the thermal energy to drive the permeation of pure water through a hydrophobic membrane and to activate the perovskite [18].

Strontium ferrates-based materials belong to a class of perovskite-type compounds in which iron is mainly stabilized as Fe^{4+} [22]. When doped with Cerium at the Sr site, the cubic structure is stabilized and the redox couple Fe^{4+}/Fe^{3+} plays a fundamental role in the functional properties of the strontium ferrates. Solution Combustion Synthesis has been frequently used for the synthesis of Ce-doped $SrFeO_3$ powders due to its versatility and efficiency in terms of energy, time, and effort [23]. However, the large number of synthesis parameters that can be changed in this synthesis can either be considered as an advantage or as an obstacle to the preparation of reproducible and efficient materials, given that a preliminary investigation of the synthesis-structure-properties relationships is missing. In this work, detailed information about the main issues that might be faced in the

solution combustion synthesis and testing of Ce-doped $SrFeO_3$ perovskite thermocatalysts is given. The effect of the specific synthesis and processing parameters on the structure, surface, redox behavior, and texture was investigated in order to select the best conditions to obtain an optimized powder. Moreover, the testing procedure was also studied and applied using different samples in order to get reliable information on their thermocatalytic behavior, highlighting the paramount importance of the reproducibility of the synthesis and procedures in the interpretation of the scientific results and the need to create reliable protocols for the synthesis and testing of the materials.

Assessing the synthesis-structure-properties relationships of such materials could open a new technology-oriented field, aiming at preparing reproducible and scalable materials, suitable for being activated at relatively mild temperatures and, in the perspective of application at real scales, exploiting the residual heat which is often available in an industrial context.

2. Results and Discussion

2.1. Synthesis and Characterization

The reproducibility of a solution combustion synthesis technique largely depends on the understanding of which preparation parameters influence the properties of the final material. Therefore, a deep knowledge on the synthesis-properties relationships is mandatory. Additionally, a reliable scale up process requires a high degree of reproducibility to maintain the same material performance observed at the lab scale. In addition, an accurate characterization protocol and a knowledge of the variability in the characterization results helps in determining the real differences among the materials. Therefore, the effect of the synthesis and processing parameters was investigated to ensure high reproducibility of the powder properties. A complementary structural and redox characterization was also performed to check the extent of variability in the characterization results.

2.1.1. Effect of the Synthesis Parameters

A series of powders with the same (or slightly different) nominal composition, $Sr_{0.86}Ce_{0.14}FeO_{3-\delta}$, but prepared using different synthesis parameters, were compared accordingly to some of their chemical–physical properties, with the aim of classifying the importance of the experimental conditions in an effort to obtain reproducible and effective catalysts. In the first comparison, two powders prepared with the same nominal composition, i.e., $Sr_{0.86}Ce_{0.14}FeO_{3-\delta}$ at pH = 7, but using two different degrees of gelification, NPW9-1000 and NPW4-1000, are shown. The use of pH = 6–7 ensures a good interaction between citric acid and metal cations, leading to a complete incorporation of cerium dopant into the perovskite structure, as well as minimizing the addition of ammonia solution into the combustion mixture. In NPW4-1000, the gel was combusted just after its formation from the sol, whereas in NPW9-1000, the gel was left to dry for another 10 min under magnetic stirring, i.e., until the magnetic bar could no longer move due to the full densification of the gel (high gelification degree). Another powder, NPW12-1000, was prepared at pH = 7 using a higher reducer-to-oxidizer ratio, (1.6). The result was a fully dried gel with a slightly different nominal composition of $Sr_{0.85}Ce_{0.15}FeO_{3-\delta}$, where the nominal Ce content exceeded by 1 mol% the maximum solubility of cerium in $SrFeO_3$. NPW4-1000, NPW9-1000, and NPW12-1000 were thermally treated at 1000 °C for 5 h and characterized for their structural (bulk and surface) and redox properties. NPW4-1000 was thermally treated using a temperature ramp of 2 °C/min instead of 10 °C/min, in contrast to the other two samples. However, the effect of the temperature ramp was strongly dependent on the gelification degree, albeit less important than the effect of gelification degree, as will be discussed in Section 2.1.2. The bulk structural characterization results of these three samples are reported in Figure 1.
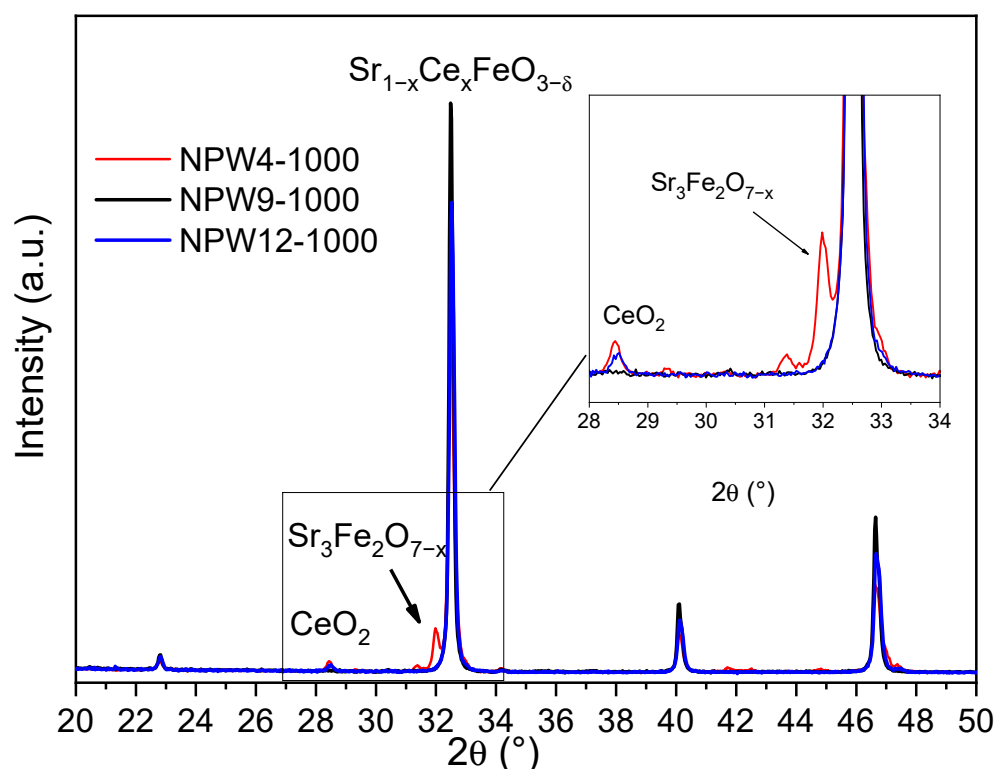
Figure 1. XRD patterns of NPW4-1000, NPW9-1000, and NPW12-1000.

The single-phase perovskite material could be obtained only for the powder prepared with fully dried gels, NPW9-1000, whereas some secondary phases were clearly visible in the sample where the gel was not completely dried, NPW4-1000 (Figure 1). These secondary phases were mainly layered tetragonal perovskites of the type $Sr_3Fe_2O_{7-\delta}$, together with minor percentages of CeO_2, formed to balance the perovskite composition after Sr and Fe segregation as layered tetragonal perovskite phases. In NPW12-1000, only the main perovskite phase was present, together with <1 wt% of segregated CeO_2, and no layered tetragonal perovskites of the type $Sr_3Fe_2O_{7-\delta}$ were formed. Despite the absence of layered tetragonal phases, segregated cerium oxide was expected for this sample, since the maximum Ce solubility in $SrFeO_3$ is lower than 15 mol% [16]. It is worth noting that the XRD pattern of NPW10-1000 (not shown), prepared using identical conditions to those of NPW9-1000, was identical to that of NPW9-1000, demonstrating the importance of controlling the gelification degree. Therefore, full gelification of the sol is a very important synthesis parameter for a good reproducibility of the structural properties, avoiding $Sr_3Fe_2O_{7-\delta}$ layered perovskite and, consequently, cerium oxide segregation.

The same three samples were characterized for their surface structure by X-ray photoelectron spectroscopy (XPS). Figure 2B shows the Sr3d, Fe2p, and O1s regions of the two samples, while Table 1 shows the binding energy and the relative abundance of the different components. The presence of cerium is evidenced by the analysis, but its low intensity and the complexity of the Ce3d peak make the region analysis unmeaningful. The Fe2p region shows a similar profile for the three samples (see Figure 2B) with the typical complex profile of the Fe2p region with the Fe2p3/-Fe2p1/2 separation of 13.3 eV and the presence of a small shake up feature.
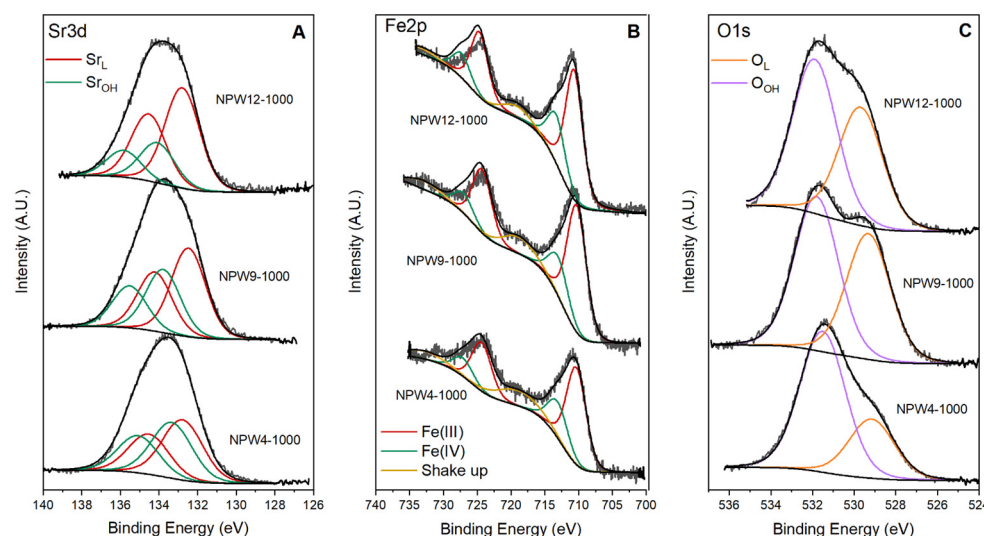
Figure 2. (**A**) Sr 3d 5/2, (**B**) Fe2p3/2 and (**C**) O1s XPS regions for NPW4-1000, NPW9-1000, and NPW12-1000.

Table 1. Binding energy and relative abundance of the different components of the Sr 3d 5/2, Fe2p3/2 and O1s XPS regions for NPW4-1000, NPW9-1000, and NPW12-1000 powders.

Sample	Sr 3d 5/2	Fe2p3/2	O1s
NPW4-1000	132.8 (52%)	710.3 (76%)	529.1 (30%)
	133.3 (48%)	713.0 (24%)	531.5 (70%)
NPW9-1000	132.5 (58%)	710.3 (73%)	529.3 (45%)
	133.8 (42%)	713.1 (27%)	531.8 (55%)
NPW12-1000	132.8 (71%)	710.7 (73%)	529.7 (43%)
	134.1 (29%)	713.3 (27%)	531.9 (57%)

The main peaks can be deconvoluted into two components at ca. 711 and 713 eV, which are attributed to Fe(III) and Fe(IV), respectively [24,25]. The relative percentage of the two species does not change along the series. The Sr3d region shows a peak, which is a convolution of Sr3d5/2 and Sr3d3/2 (DE = 1.8 eV), as evidenced in Figure 2A. The shape of the peak points to the presence of two doublets with the Sr3d5/2 centered at ca. 132.5 eV and 134 eV, which, according to the more common interpretation, may be attributed to Sr in the perovskite structure (Sr_L) and $SrCO_3$ (strontium carbonate), respectively [26–28]. $SrCO_3$ is often formed in $SrFeO_3$-based compounds due to the high affinity of Sr for atmospheric CO_2, especially in the presence of humidity [29]. The O1s region is characterized by two components (Figure 2C): O_L, at 529.6 eV, is attributed to oxygen in the perovskites lattice, while and O_{OH}, at 531.5 eV, is attributed to adsorbed oxygen species and/or carbonates [25,30]. Differences in the ratio between the two oxygen components may be indicative of differences in the oxygen vacancies present in the materials, even though due to the presence of carbonates, the correlation is not straightforward. NPW4-1000 has the smallest O_L/O_{OH} ratio. However, this does not indicate a higher number of oxygen vacancies present in the structure, but a higher percentage of $SrCO_3$ species at the surface (Figure 2 and Table 1). Therefore, it seems that the presence of secondary phases in the bulk, as detected by XRD, favors the formation of carbonate on the surface, and this could negatively affect the thermocatalytic activity, as recently observed in the literature [29]. Looking at the XPS data, NPW9-1000 and NPW12-1000 showed similar O_L/O_{OH} ratios, indicating that the oxygen surface distribution remained identical, although less surface carbonate formation occurred.

The redox properties of the three samples were investigated using TPR, TPO, and TPD techniques. The characterization results are shown in Figure 3. The TPR profile of the single-phase powder, NPW9, is characterized by two main peaks: the first one centered at 455 °C and the second one above ~750 °C, with a maximum at around 1000 °C (Figure 3A). According with our previous investigation of Ce-doped strontium ferrates [31], the low

temperature peak is ascribed to the reduction of Fe^{4+} species, typically present in the perovskite, to Fe^{3+}, while in the region 550–700 °C, the reduction of Ce^{4+} may occur, and above 700–750 °C, reduction of Fe^{3+} to Fe^{2+} and eventually to Fe^0 takes place. Similar reduction profiles were registered for the other two samples, NPW4-1000 and NPW12-1000, with both containing minor percentages of segregated phases as $Sr_3Fe_2O_{7-\delta}$ layered perovskites. In both cases, a shift of the first main reduction peak at low temperature occurred; this effect was more important for NPW12-1000. Therefore, the presence of the segregated layered perovskite phases in NPW4-1000 had a positive effect on the oxygen vacancies availability at lower temperatures, although the most important improvement was for NPW12-1000, due to the use of an over-stoichiometric reducers-to-oxidizers (Φ) ratio (1.6) and the presence of segregated ceria phase. The TPO curves, registered on the samples reduced up to ~1000 °C (Figure 3B), show very similar profiles with two main peaks: the first at around 200 °C and the second one at 380–400 °C. The curves for NPW9-1000 and NPW12-1000 are overlapping, while the reoxidation for the reduced phases formed in NPW4-1000 seems to occur at slightly higher temperatures than for the previous two, indicating that the reduced Fe-containing phases formed upon the previous reduction treatment (TPR) were slightly more stable in NPW4-1000 than in the other two samples. The TPD curves registered after the TPO (Figure 3C) for all the three samples showed desorption peaks at around 335–360 °C. According to the literature, such peaks correspond to the desorption of suprafacial α-species [32]. The sample NPW4-1000 was characterized by the highest desorption peak, suggesting the presence of the highest amount of active surface oxygen species that can be easily released at relatively low temperature (starting from 250 °C, with a maximum at 335 °C) and, therefore, that could better participate in a thermal oxidation reaction.
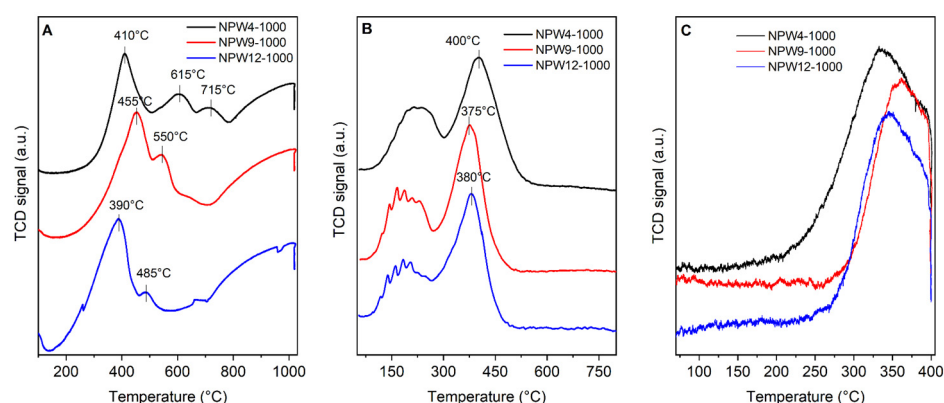

Figure 3. TPR (**A**), TPO (**B**) and TPD (**C**) profiles of NPW4-1000, NPW9-1000, and NPW12-1000 samples.

Looking at the comparison of the redox properties of NPW4-1000, NPW9-1000, and NPW12-1000, the presence of segregated perovskite layered phases could favor the interaction with polar substrates, thereby inducing a better catalytic activity of the material. In order to investigate this aspect, another powder was considered: NPW6-1000 was prepared under conditions similar to those applied for NPW4-1000, with changes in pH and gelification degree. These modifications (namely, a pH value of 6 and a medium degree of gelification) should guarantee the formation of layered perovskite and segregated ceria, as confirmed by XRD measurements, in addition to the increase of perovskite fraction and maximization of absorbance response. Similarly, NPW6-1000 contains a smaller amount of layered perovskite phase with respect to NPW4-1000 (see Table 2). This sample was analyzed by FTIR spectroscopy and the related spectra, reported in Figure 4, show the scattering profile typical of a nanopowder, with signals specifically related to the perovskite structure at 600 cm^{-1} and to the surface carbonate groups produced by interactions with atmospheric CO_2 at 1100 cm^{-1}. The high frequency range (3700–2500 cm^{-1}) is typically related to the presence of OH, NH, and CH vibrational features. A strong and large signal is visible in the spectra of the material, indicating that such species are present, even if a

more specific attribution of the signal was not possible, given the wideness of the band. To verify that these groups were actually exposed at the sample surface, a contact with D_2O vapor pressure was performed in order to exchange the hydrogen atoms in the OH, NH, and CH groups with deuterium, with consequent modification of the spectra profile. No modification of the signals was observed, indicating that their concentration at the surface of the material was very low or that the hydrogenated groups were not reachable by D_2O molecules and, therefore, these groups, if present, were in the bulk of the material or under its surface.

Table 2. Details of the synthesis condition and relevant chemical–physical features of the investigated Ce-doped $SrFeO_3$ samples.

| Sample/ Ce mol%	Synthesis Conditions (Reducers-to-Oxidizers Ratio, pH, Gelification Degree and Laboratory)	Processing Conditions (calcination Temperature and Heating Ramp)	BET Specific Surface Area (m^2/g)	Phase Composition (from Rietveld Refinement)		
				$Sr_{0.86}Ce_{0.14}FeO_3$ Amount (% wt)	CeO_2 Amount (% wt)	$Sr_3Fe_2O_{7-\delta}$ Phase Amount (% wt)
NPW9_1000/ 14 mol%	1 7 High Lab B	1000 °C/5 h, 10 °C/min	nd	100	0	0
NPW4-1000/ 14 mol%	1 7 Low Lab B	1000 °C/5 h, 2 °C/min	~1	88.4	1.6	10
NPW3-1000/ 14 mol%	1 7 High Lab B	1000 °C/5 h, 2 °C/min	~1	99	1	0
NPW6-1000/ 14 mol%	1 6 Medium Lab B	1000 °C/5 h, 2 °C/min	~1	93.4	1.6	5
NPW10-1000/ 14 mol%	1 7 High Lab B	1000 °C/5 h, 10 °C/min	~1	100	0	0
NPW12-1000/ 15 mol%	1.63 7 High Lab B	1000 °C/5 h, 10 °C/min	~1	99	1	0
NPW13-1000_A/15 mol%	1.63 6 High LabA	1000 °C/5 h, 5 °C/min	~1	98	2	0
NPW13-1000_B/15 mol%	1.63 6 High Lab B	1000 °C/5 h, 10 °C/min	~1	98	2	0
NPW13-NC/ 15 mol%	1.63 6 High Lab B	No thermal treatment (as-combusted powder)	~6	94	0	4 ($SrCO_3$) 2 (Fe_3O_4)
NPW13-800/ 15 mol%	1.63 6 High Lab B	800 °C/2 h, 10 °C/min	~4	98.8	1.2	traces ($SrCO_3$)
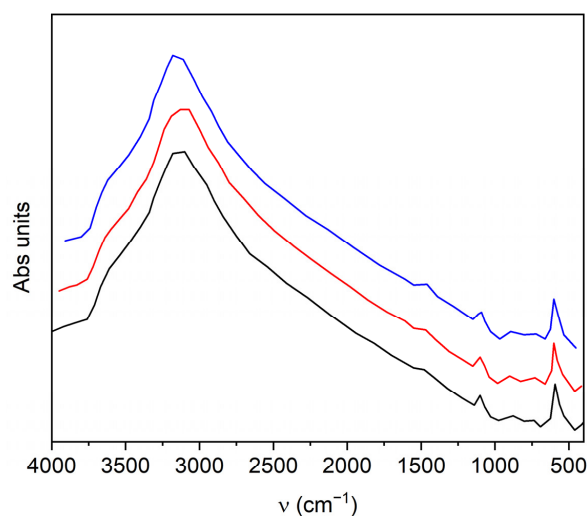
Figure 4. FTIR absorbance spectra of NPW6-1000 in air (black curve), after 1 min outgas (red curve) and after 30 min outgas (blue curve). The curves were shifted along the y-axis to better display the spectra details.

For the identification of surface active sites, the powders, after pre-activation in a vacuum at 30, 150, 300, 400, 500, 600, and 700 °C, were contacted with the CO, NO, and CO_2 gaseous probes in order to study the surface Lewis acidity of the material given by cationic species, which is prone to establishing specific interactions with the probe molecules (for instance, it is known that CO and NO show a very important affinity with Fe^{n+}, whereas CO can establish important interactions with Ce^{4+}). In no case did the probe molecules show visible interactions with the material, suggesting a limited concentration of the adsorbing surface sites and confirming again that the exposed surface of the material was very limited. Additionally, gaseous O_2 was used as a probe to check the redox behavior of the material, considering that activation in vacuo at high temperature favors the reduction of the perovskite, inducing a consequent interaction with molecular oxygen. The interaction was studied by microgravimetry. The results of the test performed on NPW6-1000 sample outgassed at RT, 150, 300, and 400 °C are reported in Figure 5 and indicate a limited interaction of the material with O2, increasing with the temperature of the preliminary outgassing of the sample. The uptake on the sample treated at 300 and 400 °C was similar, indicating that the activation of the sample at 400 °C did not significantly change the O_2 interaction properties of the material.
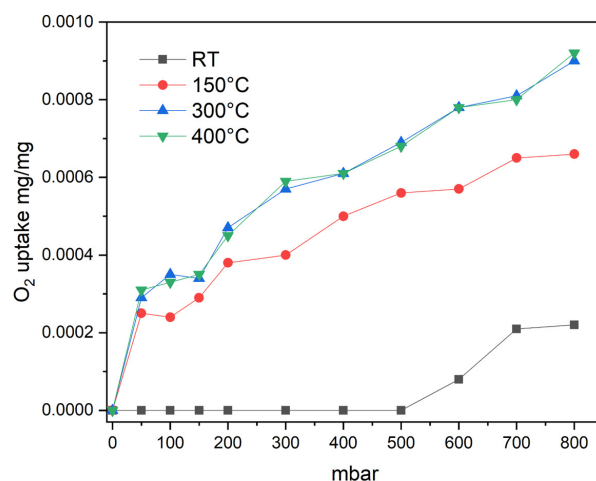

Figure 5. Microgravimetric O_2 uptake with NPW6-1000 activated in vacuo at RT (nearly 30 °C), 150, 300, and 400 °C.

2.1.2. Effect of the Processing Parameters

　　The same batch of as-burned powder was divided in two portions and treated at 1000 °C/5 h with a different temperature ramp: 2 °C/min or 10 °C/min. The XRD patterns registered for the samples treated with different temperature ramps were slightly different for samples prepared from gels with low and medium gelification degrees, although the effect was null for samples prepared using a complete gelification. It can be hypothesized that the not fully densified gel still contained some water, whose evaporation process velocity may have affected the phase composition of the final powder. As a consequence, the applied temperature ramp value was not a parameter controlling the process if the gelification degree was high enough. From the N_2 adsorption results, it was found that all the powders showed a specific surface area of about 1 m^2/g. A washing treatment carried out by sonicating the powder in bi-distilled water for two hours, according to a procedure previously used for other perovskites prepared by the same methodology [33], did not significantly change the textural feature of the materials. At the same time, a check of the washing medium was performed to evaluate the release of unreacted precursors during sonication. Again, the total organic carbon measurements did not evidence substantial release, confirming the N_2 adsorption results. To increase the specific surface area of the materials and, consequently, the activity, the effect of the calcination temperature was studied on a sample that was prepared under optimized conditions of gelification degree, pH, and chemical composition. The comparison was done between the as-burned sample, NPW13-NC, the sample treated at 800 °C/2 h, NPW13-800, and the sample treated at 1000 °C/5 h, NPW13-1000_B. NPW13_NC shows a specific surface area of about 6 m^2/g, i.e., slightly higher than that of NPW13-800 (about 4 m^2/g), which is slightly higher than that of NPW13-1000 (about 1 m^2/g). This trend may reflect both a modification of the crystal size during the calcination process (increasing from 71 nm to 150 nm with the increase of calcination temperature) or the presence of unburned precursors that may have contributed to the increase of the area of non-calcined or 800 °C-calcined samples. [23]. Beside the slight change in the surface area, the perovskite was present as the main phase at all the firing temperatures, although some $SrCO_3$ was clearly visible in the non-calcined sample and in the 800 °C-calcined sample (traces), whereas segregated CeO_2 was visible in both the calcined samples, although the CeO_2 peaks of the 800 °C-calcined sample were very large (Figure 6 and Table 2).
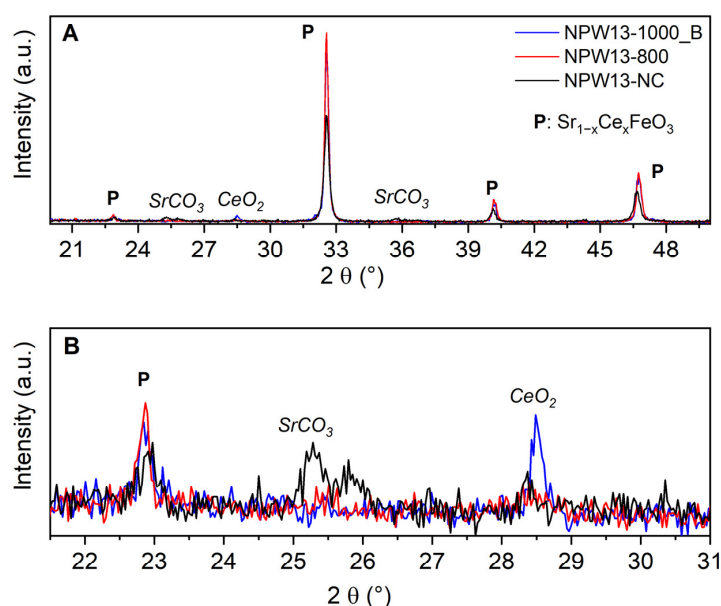

Figure 6. (**A**) XRD patterns of NPW13-NC, NPW13-800, and NPW13-1000_B; (**B**) an inset of the 21.5–31° 2θ region showing the secondary phases.

2.2. Testing Procedures

2.2.1. Effect of pH on Perovskite Stability and Metal Leaching

The results of the stability tests performed on the sample NPW13-1000_A are reported in Figure 7. NPW13-1000-A was chosen for this test as it is one of the most active thermocatalysts studied (see Section 2.2.2), for which the definition of the stability pH range could be interesting for the future applications. Strontium was released in the entire examined range of pH, but the most dramatic situation was observed at pH $\approx$ 2, where Sr, Ce, and Fe were all released in solution. Interestingly, the ratio between the amount of Sr and Ce released in solution at that pH was almost the same as that calculated for the perovskite phase (Sr/Ce = 0.86/0.14), whereas the amount of Fe released was much lower than expected, probably because it forms insoluble species.
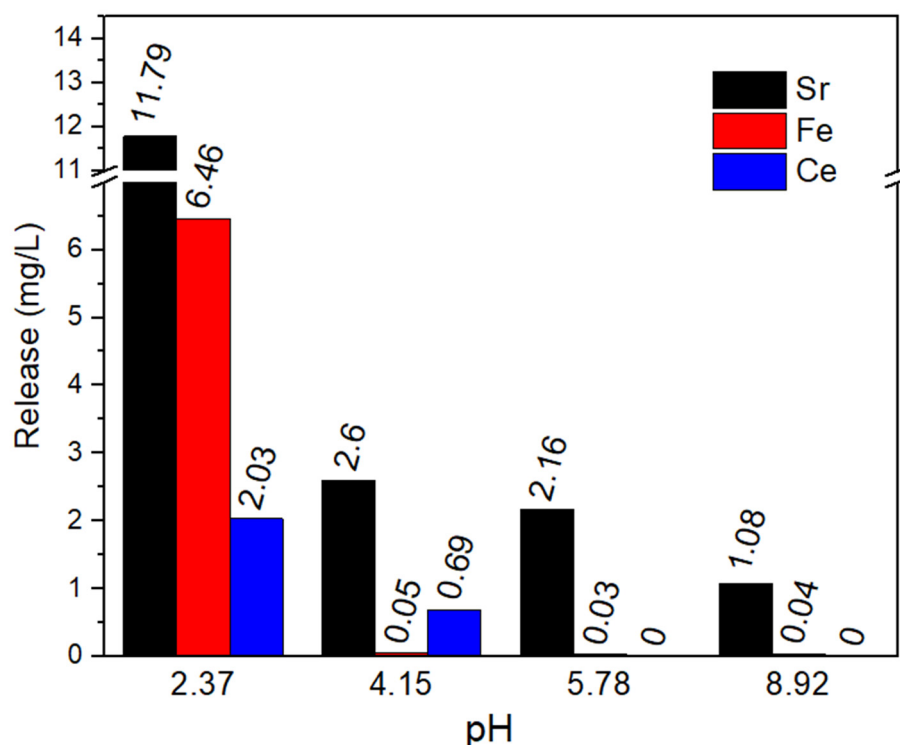

Figure 7. Sr, Fe, and Ce concentrations in solution released from perovskite at different pH values, for the NPW13-1000_A sample.

Apart from a small amount of strontium released at pH > 5, the results indicate a good material stability and suggest a possible use on pollutant removal from freshwater sources, whose pH generally ranges between 6 and 8. Otherwise, these materials seem to be not suitable for applications requiring acidic media (pH lower than 4), e.g., for the treatment of waters contaminated by inorganic contaminants.

2.2.2. Effect of the Experimental Conditions Used for the Thermocatalytic Tests

The thermocatalytic performance of the Ce-doped SrFeO$_3$ perovskite was studied on a sample prepared under optimized conditions of gelification degree, pH, and chemical composition, and subjected to different thermal treatments. To this end, Orange II (OII) and bisphenol A (BPA) were selected as model contaminants. All experiments were performed at the pH obtained after the solubilization of the target pollutant and the suspension of the perovskite. The obtained pH values typically ranged between pH 9 and 10. The strong solution basification driven by these perovskites was likely due to protonation/deprotonation equilibria at the surface of the catalyst, as confirmed by the behavior that was already reported in the literature for similar materials [16]. Control experiments at room temperature, as well as adsorption tests, were also performed, followed by degradation experiments

after raising the temperature to 70 °C. Using Orange II (OII), no degradation was observed after 200 min of contact at 70 °C with NPW6-1000, NPW10-1000, and NPW12-1000, while a different trend was observed when using the samples prepared under optimized conditions, as reported in Figure 8.
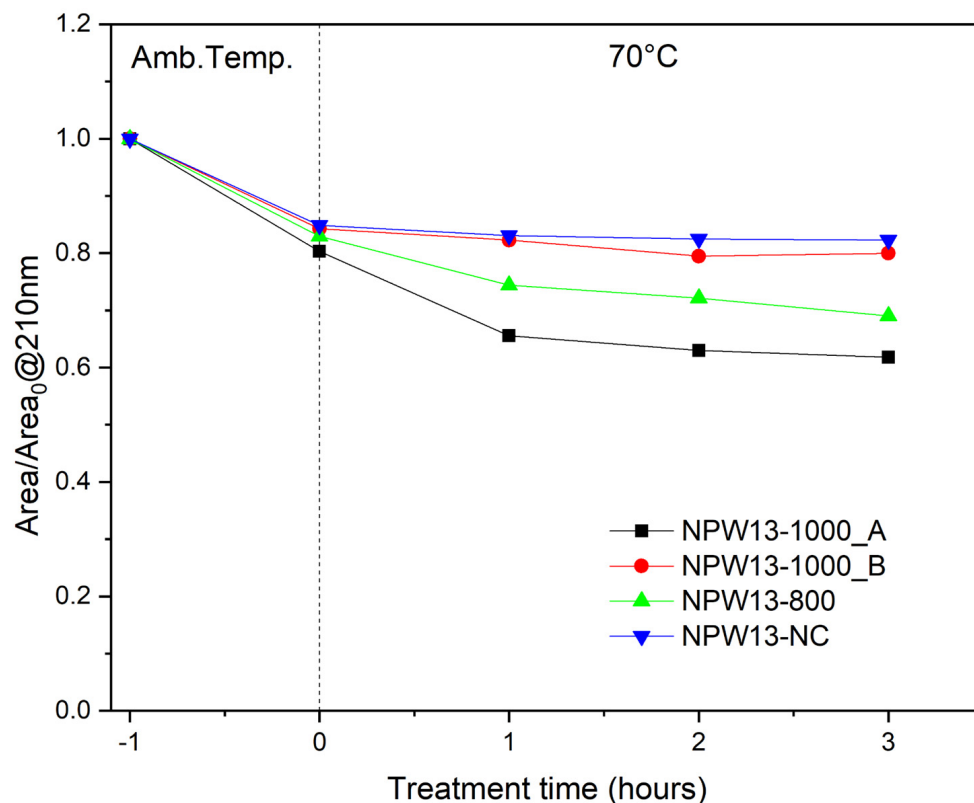

Figure 8. Orange II degradation vs. contact time in the presence of NPW13-NC and NPW13 calcined at different temperatures and prepared by Lab B, in comparison with NPW13-1000_A.

As can be noticed after 1 h contact at room T with OII, all the powders showed a comparable decrease in OII concentration; this can be reasonably ascribed to adsorption. Afterwards, the most efficient material was NPW13-1000_A (prepared in the laboratory A using the same synthetic procedure adopted for sample NPW13-1000_B in laboratory B), followed by NPW13-800, whereas NPW13-NC, and NPW13-1000_B were negligibly able to promote OII degradation.

A similar behavior was observed when testing the material with BPA, as can be observed in Figure 9. Figure 9 reports a quite odd shape of the curves, with an unexpected change at about 2 h of reaction time. The action of the thermocatalysts was stimulated at 60–70 °C; these conditions could facilitate the desorption of initially adsorbed compounds, resulting in the odd trend observed in Figure 9 after around 2 h of reaction time. Once the system had stabilized, because the abatement approaches the steady step, a normal trend returned and the curves became similar to what one would expect for all the samples except for NPW13-NC. This sample was not submitted to a post-synthesis calcination and the relative trend observed confirms that the calcination of the system makes it possible to clean the material of possible unburned precursors affecting the reaction and standardizes the product for its subsequent application.
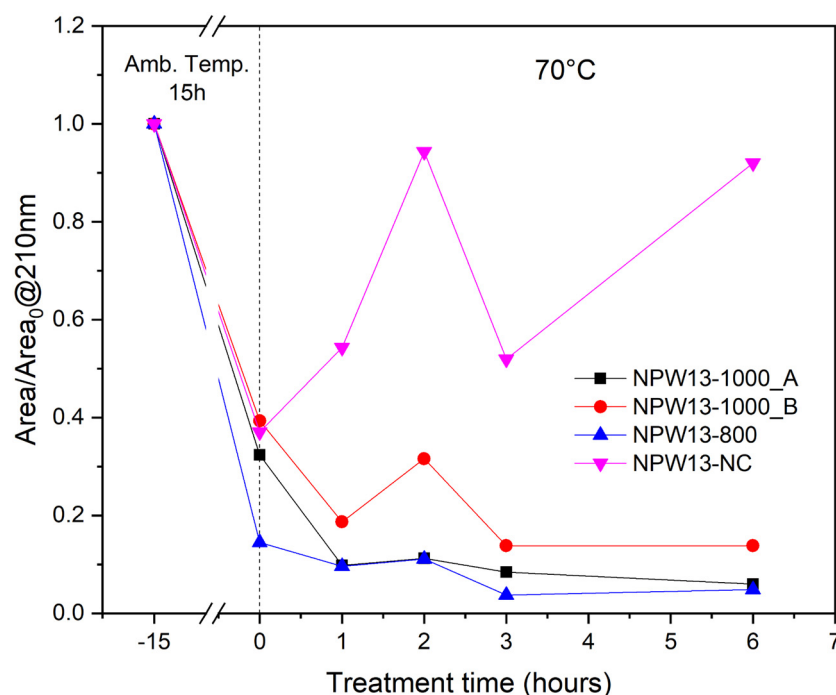
Figure 9. Degradation of BPA 5 mg/L in the presence of NPW13-NC and NPW13 calcined at different temperatures and prepared by Lab B, in comparison with NPW13-1000_A.

However, with BPA, the contact time at room T was prolonged to 15 h and the percentage of BPA decrease was higher than the one observed for OII that was kept in contact at room T with the perovskite for only 1 h before raising the T. It is reasonable to consider that more adsorption took place after 15 h at ambient temperature, also considering the absence of secondary peaks in the HPLC profiles. However, we cannot exclude the possibility that the material had already catalyzed the BPA degradation during the preconditioning, in agreement with the observed reactivity of the material at room temperature (see next discussion on Figure 10A). In contrast, at 70 °C, the further BPA decrease corresponded to the appearance of a new peak in the HPLC profile, thus indicating that BPA had undergone degradation.
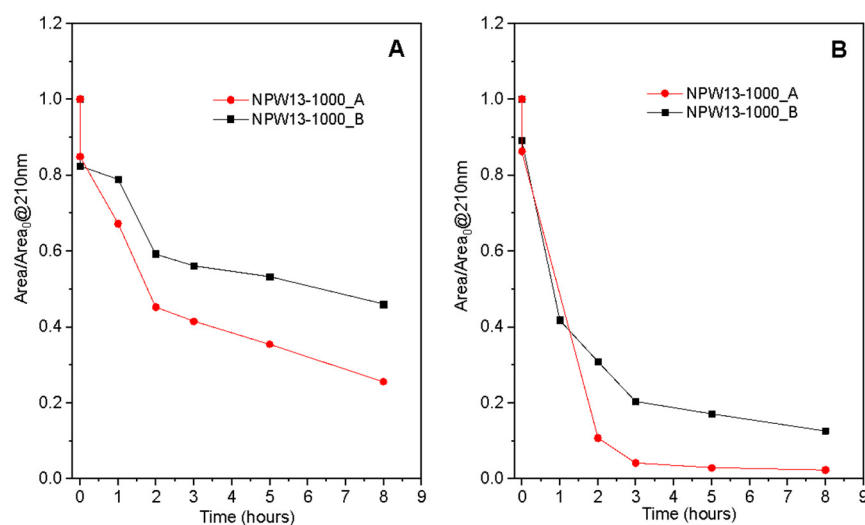

Figure 10. Difference in the performances of BPA degradation at ambient T and at 70 °C of two NPW13-1000 powders prepared following the same procedure but in two different laboratories (**A**,**B**).

Further experiments were performed using BPA as a target compound in the presence of NPW13-1000_A or NPW13-1000_B in order to compare the thermocatalytic performance of these two nominally identical materials prepared in different laboratories. BPA was again added at an initial concentration of 5 mg/L, and two series of experiments, at room temperature and at 70 °C, were performed. In both scenarios, the sample prepared in laboratory A had better performances, removing after 8 h of treatment 70% of BPA at room temperature (Figure 10A) and reaching almost complete BPA removal at 70 °C (Figure 10B).

Both batches could promote the thermal degradation of BPA at room temperature and at 70 °C, although there was a surprising and not negligible difference in their efficiency. The possible causes for this, beside the temperature ramp of 5 °C/min, may be the use of glass beaker by laboratory A and a stainless-steel beaker by laboratory B (which better retains the heat during combustion), to the beaker geometry, to the laboratory temperature during combustion, and to the technical characteristics of the muffle furnace.

To get insights on the possible species involved in the thermocatalytic process and how the presence of segregated phases can influence those species, the formation of catalyzed ROS in two samples, NPW3-1000 e NPW6-1000, containing different amount of segregated layered perovskite phases, was studied by EPR spectroscopy. In analogy with a previous study on the properties of $Sr_{0.85}Ce_{0.15}FeO_{3-\delta}$ perovskite [16], our investigations were performed at different temperatures and in the presence of a specific spin-trap (DMPO for hydroxyl radicals and TMP for singlet oxygen). The experiments in the presence of DMPO seemed to indicate, for both samples, the generation of a similar amount of hydroxyl radicals when heated at 70–75 °C, regardless of the presence of secondary phases. As shown in Figure 11, the correspondent EPR signal intensity was time-dependent, and a maximum was reached after about two hours of heating for both the samples, in agreement with the results obtained for NPW13-1000_A and close to the results obtained for NPW13-1000_B (Figure 10B). In the inset of Figure 11, the spectra are shown at 25 and 50 °C after 2 h of heating in the presence of NPW6-1000 in order to demonstrate the absence of appreciable concentrations of DMPO-OH$^{\bullet}$ adduct in these conditions. Similar experiments performed in the presence of TMP did not lead to the appearance of any EPR signal, which was indicative of a lack of singlet oxygen formation in these conditions.
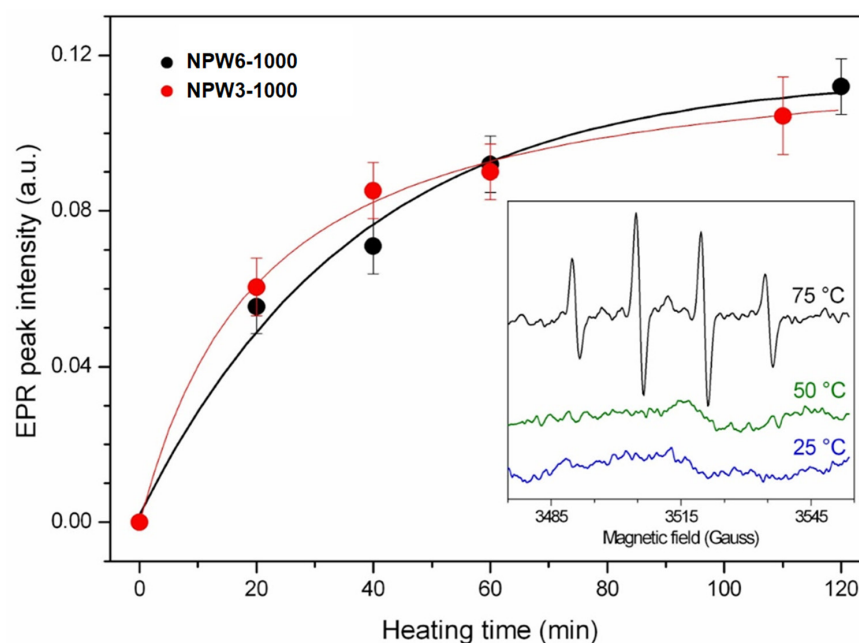

Figure 11. Intensity of DMPO-OH·EPR spectra of NPW3-1000 (red circles) and NPW6-1000 (black circles) at different heating times (inset: EPR spectra obtained with NPW6-1000 after 120 min heating at different temperatures).

3. Materials and Methods

3.1. Perovskite Oxides Synthesis

Ce-doped $SrFeO_3$ powders were obtained by solution combustion synthesis using different synthesis and processing parameters. The general methodology is described elsewhere [16]. Briefly, iron, strontium, and cerium nitrates were dissolved in distilled water in the presence of citric acid as a reducer/complexing agent/microstructural template. pH was regulated by adding ammonia solution (30 vol%) and the reducer-to-oxidizer ratio was regulated by adding ammonium nitrate as an additional oxidant, maintaining a citric acid-to-metal cation ratio of 2. The combustion mixture was left to evaporate until a gel was formed and the combustion process was initiated on the gel by setting the hotplate temperature to about 300 °C. The varied parameters were pH, gelification degree, calcination temperature/ramp, reducers-to-oxidizers ratio, and Ce nominal amount in mol%. The applied reducer was citric acid, whereas oxidizers were metal nitrate precursors and ammonium nitrate as an additional oxidant.

Gelification degree was evaluated qualitatively as follows:

(i) low: the gel is still fluid at 80 °C and densifies only after it is left at room temperature;

(ii) medium: the gel is only partially densified at 80 °C and the magnetic stirrer can still rotate and mix the gel;

(iii) high: the gel is fully densified already at 80 °C and the magnetic stirrer is blocked and cannot mix the gel anymore.

Most of the samples were calcined at 1000 °C for 5 h after the synthesis to remove any unreacted precursor and any residual carbon formed from incomplete citric acid combustion, to allow the perovskite to fully form, and to allow the Sr from $SrCO_3$ to be fully incorporated in the perovskite structure. In addition, one sample was left uncalcined, while another sample was calcined at 800 °C/2 h.

Referring to Table 2, the applied synthesis conditions allowed us to obtain materials containing (i) $Sr_{0.86}Ce_{0.14}FeO_3$ as the unique phase (NPW9-1000 and NPW10-1000), (ii) $Sr_{0.86}Ce_{0.14}FeO_3$ as the main phase together with low percentage of CeO_2 as segregated oxide (NPW12-1000, NPW3-1000, NPW13-1000_B), or (iii) $Sr_{0.86}Ce_{0.14}FeO_3$ as the main phase together with low percentage of CeO_2 as segregated oxide and of another secondary phase in variable amounts (NPW4-1000, NPW6-1000). Additionally, the effect of the post-synthesis calcination treatment was considered when comparing the features of the sample prepared under optimized conditions with those of the as burned sample (no calcination) (NPW13-NC) and after calcination (ramp 10 °C/min) for 2 h at 800 °C (NPW13-800) or for 5 h at 1000 °C (NPW13-1000_B). The optimized conditions used for NPW13-1000_B were coincident with the ones applied in a previous paper [16]. Finally, a sample was prepared by some of the authors in another laboratory (called Laboratory A) following the same procedure used for NPW13-1000_B (prepared in the Lab B) but using a temperature ramp of 5 °C/min, and was named NPW13-1000_A (prepared in the Lab A).

3.2. Perovskite Oxides Characterization

X-ray diffraction (XRD) measurements were carried out on a Bruker-Siemens D5000 X-ray powder diffractometer equipped with a Kristalloflex 760 X-ray generator and with a curved graphite monochromator using Cu Kα radiation (40 kV/30 mA). The 2θ step size was 0.03, the integration time was 20 s per step, and the 2θ scan ranged from 10° to 90°. The powder diffraction patterns were analyzed by Rietveld refinement using the GSAS II software [34]. The compound $Sr_{0.9}Ce_{0.1}FeO_3$ (ICDD PDF4+ inorganic database—PDF Card n° 04-014-0169) was chosen as a starting model for the Rietveld Refinement, setting the Sr and the Ce occupancies to 0.86 and 0.14, respectively. A Chebyschev polynomial function with eight polynomial coefficients was chosen for the background, and the Pseudo Voigt function was used for the peak profile fitting. In the structure refinement lattice constants, Debye Waller factors, microstrain, and crystal size were considered as variable parameters. Crystal size was obtained directly from the GSAS II software output based on the Scherrer equation, while microstrain is a unitless number obtained directly

from the GSAS II software output and describing a range of lattice constants through the equation $10^{-6} \cdot (\Delta\text{-d})/\text{d}$. From the fitting results, the structural parameters of the investigated compounds and the phase composition and the relative cell edge lengths were obtained. The agreement between fitted and observed intensities, the Rw factor, and the χ^2 were acceptable [35].

To remove and quantify the unburned carbon, the powder was suspended in MilliQ™ water (500 mg L^{-1}) and stirred for 2 h.

The specific surface area was determined by studying the gas-volumetric N_2 uptake at N_2 boiling point ($-196\,°C$) using an ASAP2020 gas-volumetric apparatus by Micromeritics. Sample analyses were performed after outgassing the materials in a vacuum (residual pressure $\sim10^{-2}$ mbar) for several hours at $100\,°C$ to achieve good surface cleaning. The BET model was applied for surface area determination.

The stability of the sample NPW13-1000_A was tested at different pH values keeping 20 mL of the powder suspensions (750 mg/L) under constant stirring for 24 h. Suspensions at pH 2, 4, and 6 were obtained via acidifying with HCl, and a test was also performed at the natural pH of the powder (pH > 8). After 24 h of contact, the suspensions were filtered and the solutions, properly acidified, and submitted to inductively coupled plasma–optical emission spectroscopy (ICP-OES Optima 7000 DV Perkin Elmer) analysis to verify the release of Sr, Fe, and Ce. This instrument was equipped with a PEEK Mira Mist nebulizer, a cyclonic spray chamber, and an Echelle monochromator. The wavelengths were 238.204, 413.764, and 407.771 nm for Fe, Ce, and Sr, respectively. Each concentration value was averaged on three instrumental measurements. A dilution (1:10) was necessary as a final step to determine Sr concentrations in all the solutions.

X-ray photoelectron spectroscopy (XPS) analyses of the powders were performed with a VG Microtech ESCA 3000 Multilab (VG Scientific, Sussex, UK), using Al Ka source (1486.6 eV) running at 14 kV and 15 mA, and in CAE analyzer mode. For the individual peak energy regions, a pass energy of 20 eV across the hemispheres was used. The constant charging of the samples was removed by referencing all the energies to the C 1s peak energy (set at 285.1 eV) arising from adventitious carbon. Analyses of the peaks were performed using the CASA XPS software (version 2.3.17, Casa Software Ltd.Wilmslow, Cheshire, UK, 2009). Gaussian (70%)-Lorentzian (30%), defined in Casa XPS as GL(30) profiles were used for each component of the main peaks after a Shirley type baseline subtraction. The binding energy values are quoted with a precision of ±0.15 eV and the atomic percentages with a precision of $\pm10\%$.

The redox properties of the perovskites were investigated by performing Temperature Programmed Reduction (TPR) and Temperature Programmed Oxidation (TPO) experiments. TPR were performed by flowing a mixture of H_2/Ar (5%, 30 mL/min) over the sample (~0.1 g) and increasing the temperature in the range between rt and $\sim1000\,°C$ (heating rate $10\,°C$/min). Experiments were carried out with a Micromeritics Autochem 2910 instrument equipped with a thermal conductivity detector (TCD). All the powders were pre-treated in O_2/He (5%, 30 mL/min) at $400\,°C$ for 1 h to remove any impurities and then cooled down under Ar atmosphere before starting the TPR. After reduction up to $1050\,°C$, the materials were cooled to room temperature under Ar and then subjected to a TPO experiment to reoxidize all the reduced species. TPO were performed as described for TPR but while flowing a mixture of O_2/He (5%, 30 mL/min) and increasing the temperature to $1000\,°C$. After TPO, the oxidized samples were cooled to rt under the same oxidizing atmosphere with the aim of keeping all the oxygen vacancies filled. Finally, a Temperature Programmed Desorption (TPD) experiment was carried out by heating the samples from rt to $400\,°C$ under He flow to desorb the "suprafacial" chemisorbed oxygen species.

3.3. Thermocatalytic Tests and EPR Measurements

For the thermocatalytic tests, aqueous suspensions of perovskite materials (750 mg L^{-1}) and substrate, Orange II (sodium salt, >85%) or Bisphenol A (>95%), 5 mg L^{-1}, were

prepared with Milli-Q™ ultrapure water, placed in ultrasonic bath for 30 s, and then stirred for 30 min to homogenize the suspension before treatment. The thermal treatments were performed using 50 mL of suspension in closed Pyrex® cells under continuous stirring in a thermostatic bath maintained at 70 °C; control dark tests at room temperature were also conducted. After different times, the samples were taken and filtered on a PTFE membrane using syringe Minisart® and Syringe Filters 0.45 μm. The compound disappearance was followed by HPLC-UV using a Merk Hitachi L-6200 system coupled with a UV-Vis L-4200 detector; the column used was a RP-18 (5 μm) LIChrospher® 100 Merck (125 × 4 mm). Compound detection was performed at the wavelength of maximum absorbance of each compound (484 nm for OII and 225 nm for BPA) under isocratic conditions using acidic ultrapure water (0.1% H3PO4) and methanol as eluents mixed in a ratio 88/12 for OII and 60/40 for BPA. Study of the reactive species was conducted by Electron Paramagnetic Resonance (EPR) in the presence of 5,5-dimethyl-1-pyrroline-N-oxide (DMPO) or 2,2,6,6-tetramethyl-4-piperidone hydrochloride (4- oxo-TMP) [36,37]. EPR spectra were recorded at rt with a X-band Bruker-EMX spectrometer equipped with a cylindrical cavity operating at 100 kHz field modulation. The acquisition parameters were as follows: frequency—9.86 GHz, microwave power—5 mW, modulation amplitude—2 G, and conversion time—30.68 msec. As previously reported [38,39], the experiments were carried out by adding the spin trap in the cell at the desired temperature; then, after the treatment, a portion of the sample was withdrawn in a capillary quartz tube and the EPR spectrum was immediately acquired.

4. Conclusions

The obtained results indicate how crucial the control of the synthetic parameters is in obtaining a material with the desired efficiency and featuring reproducible properties when different batches of the same materials are synthesized. With regards to the thermocatalytic efficiency of these materials with Orange II or BPA, the most promising ones seem to be those containing the highest amount of segregated CeO_2, i.e., NPW13-1000_A and NPW13-1000_B, probably due to the higher oxygen vacancy availability induced by the CeO_2 segregation. On the other hand, the segregation of tetragonal layered $Sr_3Fe_2O_{7-\delta}$ phases has to be avoided, since it favors $SrCO_3$ formation on the surface, with the risk of blocking the thermocatalytic reaction without causing an evident improvement in the oxygen vacancy availability. Furthermore, the surprising and not negligible difference in the thermocatalytic efficiency of two materials prepared with the same procedure but in two different laboratories evidences the sensitivity of the synthesis to the experimental set-up and instrumentation used. Despite the low surface area values of the investigated samples, a surface area increase from 1 to 5 m^2/g had a positive effect on the thermocatalytic performance. An in-depth study of the degradation pathways of contaminants and a better comprehension of the adsorption phenomena at the surface of the catalyst is still to be done. The overall picture obtained by this work confirms the potential application of perovskite materials in thermocatalytic AOPs, but, at the same time, focuses the attention on the need to fully identify the key synthetic parameters to be tuned in order to obtain materials with fully reproducible characteristics and performance.

Author Contributions: Conceptualization, A.B.P. and F.D.; validation, D.P.; investigation, D.P., E.L., G.M., V.B., L.F.L., V.L.P. and M.M.; resources, A.B.P., G.M. and F.D.; writing—original draft preparation, A.B.P., D.P. and F.D.; writing—review and editing, D.P. All authors have read and agreed to the published version of the manuscript.

References

1. Jones, E.R.; van Vliet, M.T.H.; Qadir, M.; Bierkens, M.F.P. Country-level and gridded estimates of wastewater production, collection, treatment and reuse. *Earth Syst. Sci. Data* **2021**, *13*, 237–254. [CrossRef]
2. Biel-Maeso, M.; Corada-Fernández, C.; Lara-Martín, P.A. Removal of personal care products (PCPs) in wastewater and sludge treatment and their occurrence in receiving soils. *Water Res.* **2019**, *150*, 129–139. [CrossRef] [PubMed]
3. Clara, M.; Strenn, B.; Gans, O.; Martinez, E.; Kreuzinger, N.; Kroiss, H. Removal of selected pharmaceuticals, fragrances and endocrine disrupting compounds in a membrane bioreactor and conventional wastewater treatment plants. *Water Res.* **2005**, *39*, 4797–4807. [CrossRef] [PubMed]
4. Rivera-Utrilla, J.; Sánchez-Polo, M.; Ferro-García, M.Á.; Prados-Joya, G.; Ocampo-Pérez, R. Pharmaceuticals as emerging contaminants and their removal from water. A review. *Chemosphere* **2013**, *93*, 1268–1287. [CrossRef] [PubMed]
5. Rodriguez-Narvaez, O.M.; Peralta-Hernandez, J.M.; Goonetilleke, A.; Bandala, E.R. Treatment technologies for emerging contaminants in water: A review. *Chem. Eng. J.* **2017**, *323*, 361–380. [CrossRef]
6. Miklos, D.B.; Remy, C.; Jekel, M.; Linden, K.G.; Drewes, J.E.; Hübner, U. Evaluation of advanced oxidation processes for water and wastewater treatment—A critical review. *Water Res.* **2018**, *139*, 118–131. [CrossRef]
7. Li, X.; Wang, B.; Cao, Y.; Zhao, S.; Wang, H.; Feng, X.; Zhou, J.; Ma, X. Water Contaminant Elimination Based on Metal–Organic Frameworks and Perspective on Their Industrial Applications. *ACS Sustain. Chem. Eng.* **2019**, *7*, 4548–4563. [CrossRef]
8. Anucha, C.B.; Altin, I.; Bacaksiz, E.; Stathopoulos, V.N. Titanium dioxide (TiO_2)-based photocatalyst materials activity enhancement for contaminants of emerging concern (CECs) degradation: In the light of modification strategies. *Chem. Eng. J. Adv.* **2022**, *10*, 100262. [CrossRef]
9. Castanheira, B.; Otubo, L.; Oliveira, C.L.P.; Montes, R.; Quintana, J.B.; Rodil, R.; Brochsztain, S.; Vilar, V.J.P.; Teixeira, A.C.S.C. Functionalized mesoporous silicas SBA-15 for heterogeneous photocatalysis towards CECs removal from secondary urban wastewater. *Chemosphere* **2022**, *287*, 132023. [CrossRef]
10. Senobari, S.; Nezamzadeh-Ejhieh, A. A novel ternary nano-composite with a high photocatalyitic activity: Characterization, effect of calcination temperature and designing the experiments. *J. Photochem. Photobiol. Chem.* **2020**, *394*, 112455. [CrossRef]
11. Noruozi, A.; Nezamzadeh-Ejhieh, A. Preparation, characterization, and investigation of the catalytic property of α-Fe2O3-ZnO nanoparticles in the photodegradation and mineralization of methylene blue. *Chem. Phys. Lett.* **2020**, *752*, 137587. [CrossRef]
12. Chen, H.; Motuzas, J.; Martens, W.; Diniz da Costa, J.C. Degradation of azo dye Orange II under dark ambient conditions by calcium strontium copper perovskite. *Appl. Catal. B Environ.* **2018**, *221*, 691–700. [CrossRef]
13. Mahmoudi, F.; Saravanakumar, K.; Maheskumar, V.; Njaramba, L.K.; Yoon, Y.; Park, C.M. Application of perovskite oxides and their composites for degrading organic pollutants from wastewater using advanced oxidation processes: Review of the recent progress. *J. Hazard. Mater.* **2022**, *436*, 129074. [CrossRef] [PubMed]
14. Yang, L.; Jiao, Y.; Xu, X.; Pan, Y.; Su, C.; Duan, X.; Sun, H.; Liu, S.; Wang, S.; Shao, Z. Superstructures with Atomic-Level Arranged Perovskite and Oxide Layers for Advanced Oxidation with an Enhanced Non-Free Radical Pathway. *ACS Sustain. Chem. Eng.* **2022**, *10*, 1899–1909. [CrossRef]
15. Žužić, A.; Ressler, A.; Macan, J. Perovskite oxides as active materials in novel alternatives to well-known technologies: A review. *Ceram. Int.* **2022**, *48*, 27240–27261. [CrossRef]
16. Tummino, M.L.; Laurenti, E.; Deganello, F.; Bianco Prevot, A.; Magnacca, G. Revisiting the catalytic activity of a doped $SrFeO_3$ for water pollutants removal: Effect of light and temperature. *Appl. Catal. B Environ.* **2017**, *207*, 174–181. [CrossRef]
17. Leiw, M.Y.; Guai, G.H.; Wang, X.; Tse, M.S.; Ng, C.M.; Tan, O.K. Dark ambient degradation of Bisphenol A and Acid Orange 8 as organic pollutants by perovskite $SrFeO_{3-\delta}$ metal oxide. *J. Hazard. Mater.* **2013**, *260*, 1–8. [CrossRef] [PubMed]
18. Janowska, K.; Boffa, V.; Jørgensen, M.K.; Quist-Jensen, C.A.; Hubac, F.; Deganello, F.; Coelho, F.E.B.; Magnacca, G. Thermocatalytic membrane distillation for clean water production. *npj Clean Water* **2020**, *3*, 34. [CrossRef]
19. Østergaard, M.B.; Strunck, A.B.; Jørgensen, M.K.; Boffa, V. Abatement of oil residues from produced water using a thermocatalytic packed bed reactor. *J. Environ. Chem. Eng.* **2021**, *9*, 106749. [CrossRef]
20. Bortot Coelho, F.E.; Nurisso, F.; Boffa, V.; Ma, X.; Rasse-Suriani, F.; Roslev, P.; Magnacca, G.; Candelario, V.; Deganello, F.; Parola, V. A thermocatalytic perovskite-graphene oxide nanofiltration membrane for water depollution. *J. Water Process Eng.* **2022**, *49*, 102941. [CrossRef]
21. Janowska, K.; Ma, X.; Boffa, V.; Jørgensen, M.K.; Candelario, V.M. Combined Nanofiltration and Thermocatalysis for the Simultaneous Degradation of Micropollutants, Fouling Mitigation and Water Purification. *Membranes* **2021**, *11*, 639. [CrossRef] [PubMed]
22. Tummino, M.L. $SrFeO_3$ peculiarities and exploitation in decontamination processes and environmentally-friendly energy applications. *Curr. Res. Green Sustain. Chem.* **2022**, *5*, 100339. [CrossRef]

23. Deganello, F.; Tyagi, A.K. Solution combustion synthesis, energy and environment: Best parameters for better materials. *Prog. Cryst. Growth Charact. Mater.* **2018**, *64*, 23–61. [CrossRef]

24. Wu, M.; Chen, S.; Xiang, W. Oxygen vacancy induced performance enhancement of toluene catalytic oxidation using LaFeO$_3$ perovskite oxides. *Chem. Eng. J.* **2020**, *387*, 124101. [CrossRef]

25. Hu, H.; Zhang, Q.; Wang, C.; Chen, M.; Wang, Q. Facile synthesis of CaMn$_{1-x}$Fe$_x$O$_3$ to incorporate Fe(IV) at high ratio in perovskite structure for efficient in situ adsorption-oxidation of As(III). *Chem. Eng. J.* **2022**, *435*, 134894. [CrossRef]

26. Diodati, S.; Nodari, L.; Natile, M.M.; Russo, U.; Tondello, E.; Lutterotti, L.; Gross, S. Highly crystalline strontium ferrites SrFeO$_{3-\delta}$: An easy and effective wet-chemistry synthesis. *Dalton Trans.* **2012**, *41*, 5517–5525. [CrossRef] [PubMed]

27. Kuyyalil, J.; Newby, D.; Laverock, J.; Yu, Y.; Cetin, D.; Basu, S.N.; Ludwig, K.; Smith, K.E. Vacancy assisted SrO formation on La$_{0.8}$Sr$_{0.2}$Co$_{0.2}$Fe$_{0.8}$O$_{3-\delta}$ surfaces—A synchrotron photoemission study. *Surf. Sci.* **2015**, *642*, 33–38. [CrossRef]

28. Bukhtiyarova, M.V.; Ivanova, A.S.; Slavinskaya, E.M.; Plyasova, L.M.; Rogov, V.A.; Kaichev, V.V.; Noskov, A.S. Catalytic combustion of methane on substituted strontium ferrites. *Fuel* **2011**, *90*, 1245–1256. [CrossRef]

29. Østergaard, M.B.; Strunck, A.B.; Boffa, V.; Jørgensen, M.K. Kinetics of Strontium Carbonate Formation on a Ce-Doped SrFeO$_3$ Perovskite. *Catalysts* **2022**, *12*, 265. [CrossRef]

30. Paswan, S.K.; Kumari, S.; Kar, M.; Singh, A.; Pathak, H.; Borah, J.P.; Kumar, L. Optimization of structure-property relationships in nickel ferrite nanoparticles annealed at different temperature. *J. Phys. Chem. Solids* **2021**, *151*, 109928. [CrossRef]

31. Deganello, F.; Liotta, L.F.; Longo, A.; Casaletto, M.P.; Scopelliti, M. Cerium effect on the phase structure, phase stability and redox properties of Ce-doped strontium ferrates. *J. Solid State Chem.* **2006**, *179*, 3406–3419. [CrossRef]

32. Fino, D.; Russo, N.; Saracco, G.; Specchia, V. The role of suprafacial oxygen in some perovskites for the catalytic combustion of soot. *J. Catal.* **2003**, *217*, 367–375. [CrossRef]

33. Deganello, F.; Tummino, M.L.; Calabrese, C.; Testa, M.L.; Avetta, P.; Fabbri, D.; Prevot, A.B.; Montoneri, E.; Magnacca, G. A new, sustainable LaFeO$_3$ material prepared from biowaste-sourced soluble substances. *N. J. Chem.* **2015**, *39*, 877–885. [CrossRef]

34. Toby, B.H.; Von Dreele, R.B. GSAS-II: The genesis of a modern open-source all purpose crystallography software package. *J. Appl. Crystallogr.* **2013**, *46*, 544–549. [CrossRef]

35. Toby, B.H. R factors in Rietveld analysis: How good is good enough? *Powder Diffr.* **2006**, *21*, 67–70. [CrossRef]

36. Dikalov, S.; Jiang, J.; Mason, R.P. Characterization of the high-resolution ESR spectra of superoxide radical adducts of 5-(diethoxyphosphoryl)-5-methyl-1-pyrroline N-oxide (DEPMPO) and 5,5-dimethyl-1-pyrroline N-oxide (DMPO). Analysis of conformational exchange. *Free Radic. Res.* **2005**, *39*, 825–836. [CrossRef] [PubMed]

37. Moan, J.; Wold, E. Detection of singlet oxygen production by ESR. *Nature* **1979**, *279*, 450–451. [CrossRef]

38. Bianco Prevot, A.; Avetta, P.; Fabbri, D.; Laurenti, E.; Marchis, T.; Perrone, D.G.; Montoneri, E.; Boffa, V. Waste-derived bioorganic substances for light-induced generation of reactive oxygenated species. *ChemSusChem* **2011**, *4*, 85–90. [CrossRef]

39. Avetta, P.; Bella, F.; Bianco Prevot, A.; Laurenti, E.; Montoneri, E.; Arques, A.; Carlos, L. Waste cleaning waste: Photodegradation of monochlorophenols in the presence of waste-derived photosensitizer. *ACS Sustain. Chem. Eng.* **2013**, *1*, 1545–1550. [CrossRef]